ACS Energy LETTERS

http://pubs.acs.org/journal/aelccp

Implementing Dopant-Free Hole-Transporting Layers and Metal-Incorporated $CsPbI_2Br$ for Stable All-Inorganic Perovskite Solar Cells

Sawanta S. Mali,* Jyoti V. Patil, Julian A. Steele, Sachin R. Rondiya, Nelson Y. Dzade, and Chang Kook Hong*

Cite This: ACS Energy Lett. 2021, 6, 778−788

Read Online

ACCESS | Metrics & More | Article Recommendations | Supporting Information

ABSTRACT: Mixed-halide $CsPbI_2Br$ perovskite is promising for efficient and thermally stable all-inorganic solar cells; however, the use of conventional antisolvent methods and additives-based hole-transporting layers (HTLs) currently hampers progress. Here, we have employed hot-air-assisted perovskite deposition in ambient condition to obtain high-quality photoactive $CsPbI_2Br$ perovskite films and have extended stable device operation using metal cation doping and dopant-free hole-transporting materials. Density functional theory calculations are used to study the structural and optoelectronic properties of the $CsPbI_2Br$ perovskite when it is doped with metal cations Eu^{2+} and In^{3+}. We experimentally incorporated Eu^{2+} and In^{3+} metal ions into $CsPbI_2Br$ films and applied dopant-free copper(I) thiocyanate (CuSCN) and poly(3-hexylthiophene) (P3HT)-based materials as low-cost hole transporting layers, leading to record-high power conversion efficiencies of 15.27% and 15.69%, respectively, and a retention of >95% of the initial efficiency over 1600 h at 85 °C thermal stress.

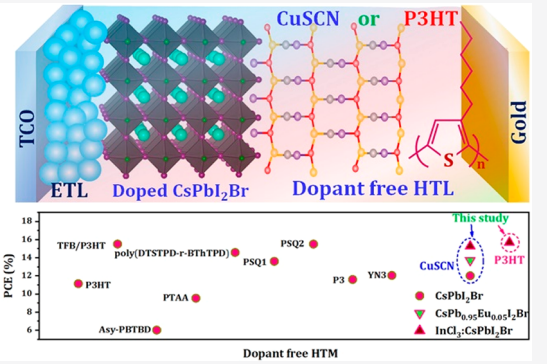

Organic−inorganic hybrid perovskite solar cells have recently demonstrated power conversion efficiencies (PCEs) exceeding 25.5%[1] using tunable, mixed halide and cation perovskite compositions.[2−7] Recent works demonstrated substantial improvement in the stability of multication organic−inorganic hybrid perovskite solar cells (PSCs) through different approaches.[8−10] However, champion devices are generally based on volatile organic cations methylammonium (MA) or formamidinium (FA) organic cations, motivating research into relatively more stable all-inorganic alternatives.[11−14] Consequently, solar cells based on $CsPbX_3$ perovskites (where X = I, Br, or Cl), and in particular iodine-rich compositions ($CsPbI_3$ band gap is ∼1.7 eV), have attracted great interest.[14] However, issues remain with regard to securing a functional $CsPbI_3$-based perovskite, because of a strong tendency for its high-temperature black phases (α, β, or γ) to destabilize to an optically inactive, nonperovskite structure (δ) under ambient conditions.[15]

Photoactive β-$CsPbI_3$ or γ-$CsPbI_3$ phases have been stabilized at room temperature using CHI-treatment and dimethylammonium iodide (DMAI) additives, demonstrating their potential for a high PCE of 19%.[13,14] Therefore, researchers are actively exploring different material compositions, with swapping I for relatively smaller Br halide atoms being a popular choice because of the resulting increase in the Goldschmidt tolerance factor.[16]

Utilizing mixed-halide $CsPbI_2Br$ perovskites is a promising avenue toward improving phase stability while retaining a solar-friendly band gap energy ($E_g \approx 1.9$ eV),[17] and they are suitable for tandem, or even triple-junction architectures.[18−20] However, the key challenge is to synthesize device-ready $CsPbI_2Br$ thin films under ambient conditions without environmentally hazardous antisolvents. Reduced dimensions,[21,22] solvent engineering strategies,[23−25] and metal ion doping[26−32] are promising approaches for stabilizing photoactive $CsPbI_2Br$ thin films, though they remain vulnerable to so-called moisture attack.[15] Alternatively, to overcome the issues associated with ambient processing, hot-air-assisted fabrication has emerged as a compelling remedy.[33−36]

Received: November 14, 2020
Accepted: December 2, 2020

https://dx.doi.org/10.1021/acsenergylett.0c02385
ACS Energy Lett. 2021, 6, 778−788

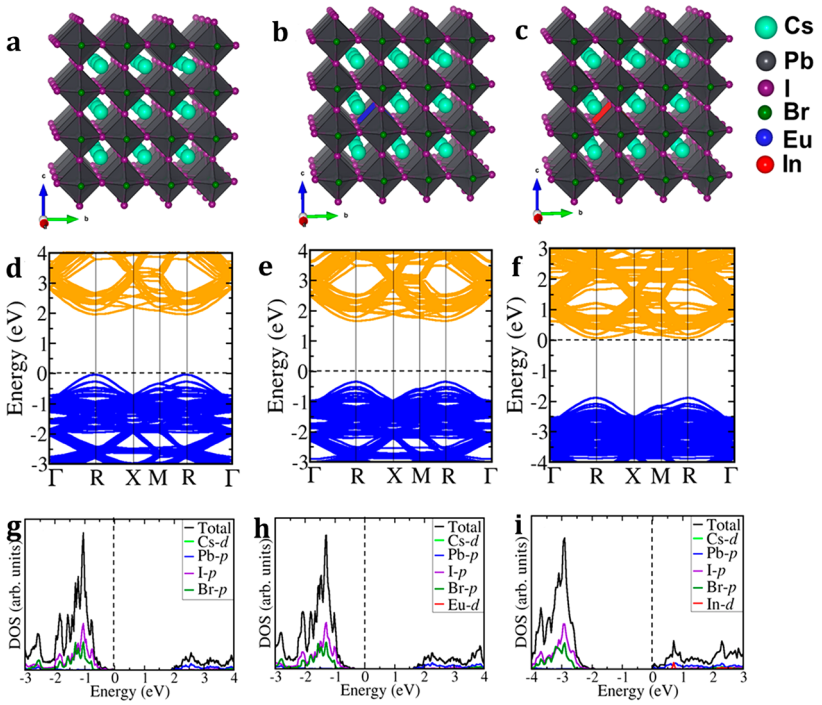

Figure 1. Schematic representation of the 3 × 3 × 3 supercell crystal structure of the (a) $CsPbI_2Br$, (b) $CsPb_{0.96}Eu_{0.04}I_2Br$, and (c) $CsPb_{0.96}In_{0.04}I_2Br$ and the corresponding (d–f) electronic band structures and (g–i) partial density of states.

Thus far, the most efficient all-inorganic perovskite solar cells have been realized using hole-transporting layers (HTLs) doped with additives which are used to regulate hole mobility and, hence, performance. For instance, poly [bis(4-phenyl)-(2,4,6-trimethylphenyl)amine] (PTAA) doped with LiTFSI (bis(trifluoromethane)sulfonamide lithium salt) and TBP (4-tertbutylpyridine) can act as efficient HTLs and have the added benefit of enhancing air stability. However, doped HTLs generally incur a high cost and increase the overall processing requirements for devices. To address this economical impairment, low-cost, dopant-free HTLs which are also hydrophobic are required.[37−39] For the case of all-inorganic $CsPbI_2Br$-based PSC, the use of poly[(dithieno[3,2-b:2′,3′-d]silolethieno[3,4-*c*]pyrrole-4,6-dione)-random-(2,2′-bithiophenethieno[3,4-*c*]-pyrrole-4,6-dione)] (poly(DTSTPD-r-BThTPD)[40] and a dopant-free donor−acceptor polymer poly(DTSTPD-r-BThTPD) have demonstrated good PCE.[41] However, the synthesis of poly(DTSTPD-r-BThTPD) is tedious and the issue of cost still remains. Therefore, alternative HTLs such as CuSCN or P3HT are a promising choice.[37,39] The use of cost-effective organic HTLs, like P3HT, are well-known to produce low open-circuit voltage (V_{OC}) due to nonradiative recombination at the poorly contacting perovskite/HTL interface.[39,42] In contrast, using highly uniform films produced via hot-air fabrication could mitigate these impairments by ensuring good contact between the layers.

Recently, Li *et al.* used P3HT for $CsPbI_2Br$-based PSC and boosted the PCE from 14.08% to 15.50% using poly[(9,9-dioctylfluorenyl-2,7-diyl)-*co*-(4,4′-(N-(4-s-butylphenyl)-diphenylamine)] (TFB) as a wide-band gap buffer layer.[43] With respect to the use of low-cost, dopant-free HTLs, the highest PCEs reached thus far are 14.08% (for $CsPbI_2Br$) and 11.8% PCE ($CsPbI_3$) using P3HT and CuSCN, respectively.[44,45] Because of its cost-effective nature, high thermal stability, and simplistic preparation, we have selected these promising dopant-free HTLs within the $CsPbI_2Br$-based PSCs we report here.

In this work, the hot-air method is used for the fabrication of pinhole-free $CsPbI_2Br$, $CsPb_{0.95}Eu_{0.05}I_2Br$, and $InCl_3$:$CsPbI_2Br$ perovskite thin films in order to improve their stability under ambient conditions. Highly uniform perovskite thin films facilitate excellent perovskite/HTL interfaces, enabling high-efficiency dopant-free HTL-based solar cells. Further incorporating Eu^{2+} and In^{3+} metal enhances device stability with PCEs recorded up to 15.27% and 15.69%, respectively, for CuSCN and P3HT HTLs. Importantly, these devices retain >95% of their initial PCE over 1600 h of operation in ambient conditions.

We begin by investigating the electronic band structures of the pristine and doped (Eu and In) $CsPbI_2Br$ materials using density functional theory (DFT) calculations (details are provided in the Supporting Information). Substituting one Pb^{2+} ion by either an Eu^{2+} or In^{3+} ion within a simulated supercell resulted in compositions $CsPb_{0.96}Eu_{0.04}I_2Br$ and $CsPb_{0.96}In_{0.04}I_2Br$, respectively (Figure 1a–c). The lattice parameter of a $CsPbI_2Br$ 3 × 3 × 3 supercell is predicted to be a = 18.903 Å, compared to the slightly smaller lattice parameter of $CsPb_{0.96}Eu_{0.04}I_2Br$ (a = 18.895 Å) and $CsPb_{0.96}In_{0.04}I_2Br$ (a = 18.878 Å), consistent with the relative change in ionic radii (Eu^{2+}, 1.12 Å; In^{3+}, 0.91 Å; and Pb^{2+}, 1.19 Å) in 6-fold coordination. The thermodynamic stability of Eu- and In-doped $CsPbI_2Br$ materials was examined by calculating the binding energy (E_b) with respect to the decomposed constituent atoms using the relation

$$E_B = \frac{(E_{total} - n_{Cs}E^{Cs}_{atom} - n_{Pb}E^{Pb}_{atom} - n_IE^I_{atom} - n_{Br}E^{Br}_{atom} - n_{Tb}E^{dopant}_{atom})}{(n_{Cs} + n_{Pb} + n_I + n_{Br} + n_{Tb})} \quad (1)$$

https://dx.doi.org/10.1021/acsenergylett.0c02385
ACS Energy Lett. 2021, 6, 778−788

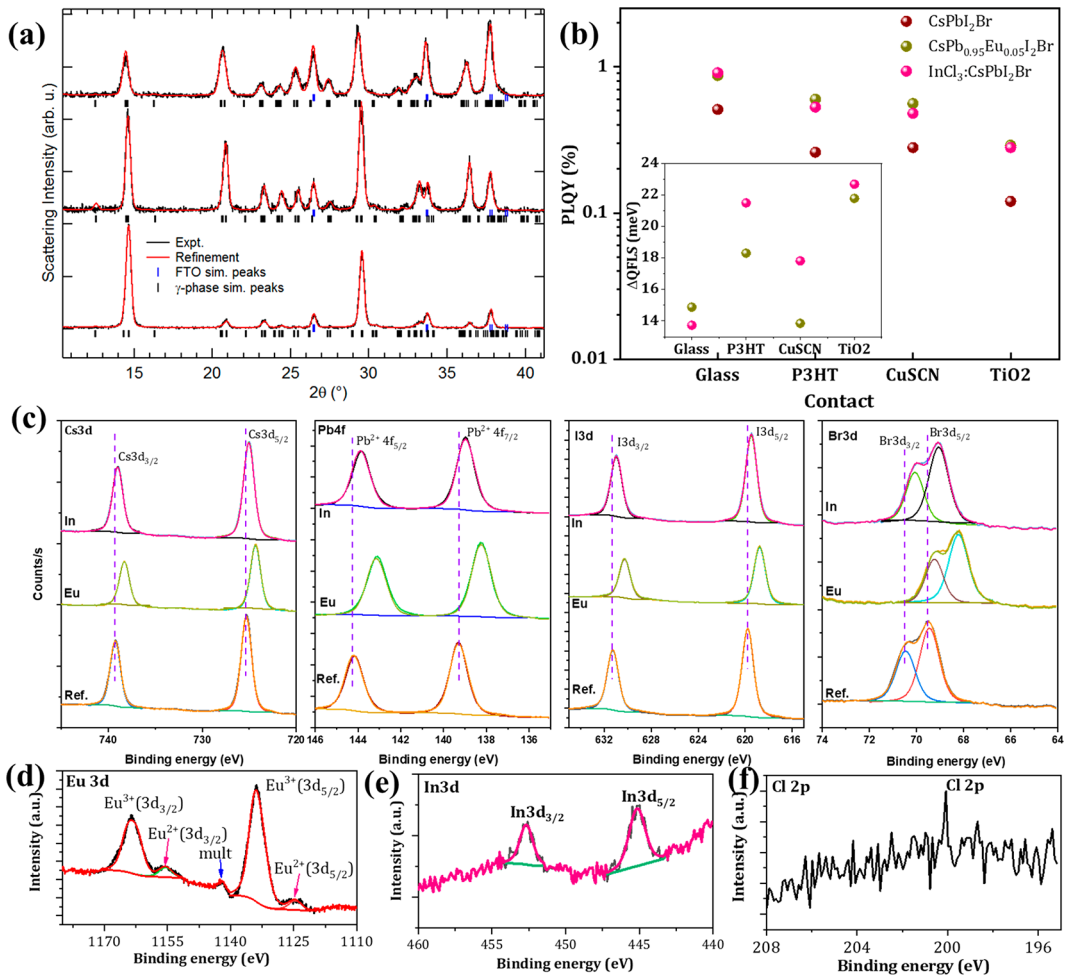

Figure 2. (a) Normalized XRD patterns and their structural refinements (Le Bail method) of γ-phase $CsPbI_2Br$-based thin films. (b) PLQY values for $CsPbI_2Br$, $CsPb_{0.95}Eu_{0.05}I_2Br$, and 0.25% $InCl_3$:$CsPbI_2Br$ thin films samples with no charge transport layer (glass) and with isolated p-type (CuSCN), p-type (P3HT) and n-type TiO_2 contacts. Inset: Improvement in QFLS as determined by eq S2 for the respective samples. (c) High-resolution XPS spectra of the Cs 3d, Pb 4f, I 3d, and Br 3d core levels for $CsPbI_2Br$, $CsPb_{0.95}Eu_{0.05}I_2Br$, and 0.25% $InCl_3$:$CsPbI_2Br$ films. (d) Eu 3d core level for $CsPb_{0.95}Eu_{0.05}I_2Br$ and (e and f) In 3d and Cl 2p core levels for 0.25% $InCl_3$:$CsPbI_2Br$ sample. Corresponding full survey scan and peak details of the fittings can be found in Table S5 and Figures S6−S8.

where E_B is the binding energy, E_{total} the total energy of pristine $CsPbI_2Br$, and E^A_{atom} the energy of the free atom i (i = Cs, Pb, I, Br, and dopant Eu or In); n_i represents the number of atom i in the supercell. The binding energies of the $CsPbI_2Br$, $CsPb_{0.96}Eu_{0.04}I_2Br$, and $CsPb_{0.96}In_{0.04}I_2Br$ are predicted to be −2.68, −2.72, and −2.71 eV per atom, respectively, indicating that Eu- and In-doped materials are thermodynamically more stable than the pristine $CsPbI_2Br$.

The calculated electronic band structures (Figure 1d−f) of $CsPb_{0.96}Eu_{0.04}I_2Br$ and $CsPb_{0.96}In_{0.04}I_2Br$ also indicate direct band gap materials, with band gap energies similar to those of the parent system (∼1.9 eV). The calculated partial density of states (Figure 1g−i) show that compared to the Eu^{2+}-doped $CsPbI_2Br$, where the Fermi level remains closer to the valence band edge, In^{3+} incorporation shifts the Fermi level closer to the conduction band edge and introduced donor states close to the bottom of the conduction band, which may be responsible for the improved electrical conductivity of In-doped $CsPbI_2Br$.[46,47] The effective masses (m^*) of holes and electrons are estimated by fitting the band edge using $m^*_{h(e)} = \pm\hbar^2\left(\frac{d^2E_k}{dk^2}\right)^{-1}$. The prediction of relatively small effective masses (Table S1) suggests high mobility of electrons and holes at the band edges and consequently points to efficient extraction of charge carriers in the pristine and doped $CsPbI_2Br$ materials.

Quality $CsPbI_2Br$ perovskite thin films were deposited by the hot-air method (Supporting Note 1 and Figures S1−S3). X-ray diffraction (XRD) analyses of the control $CsPbI_2Br$ thin film and samples doped with 5% Eu^{2+} and In^{3+} incorporation suggest only small changes in the lattice parameters. Structural refinement of the XRD data of the bare and doped $CsPbI_2Br$ confirms the formation of the common orthorhombic γ-phase perovskite (Figure 2a, Supporting Note 2, and Figure S4). Samples developed with $InCl_3$ revealed a reduced unit cell volume, although Eu doping uncovered an expanded one, which is unexpected. Nonetheless, such structural changes suggest their incorporation into the parent lattice (further structural analysis provided below).[48]

We recorded time-resolved photoluminescence (TRPL) and photoluminescence quantum yield (PLQY) from the perovskite materials deposited on glass substrates and on device-relevant substrates with isolated charge transport layers (CTLs) following a previous procedure.[49,50] With the help of

https://dx.doi.org/10.1021/acsenergylett.0c02385
ACS Energy Lett. 2021, 6, 778−788

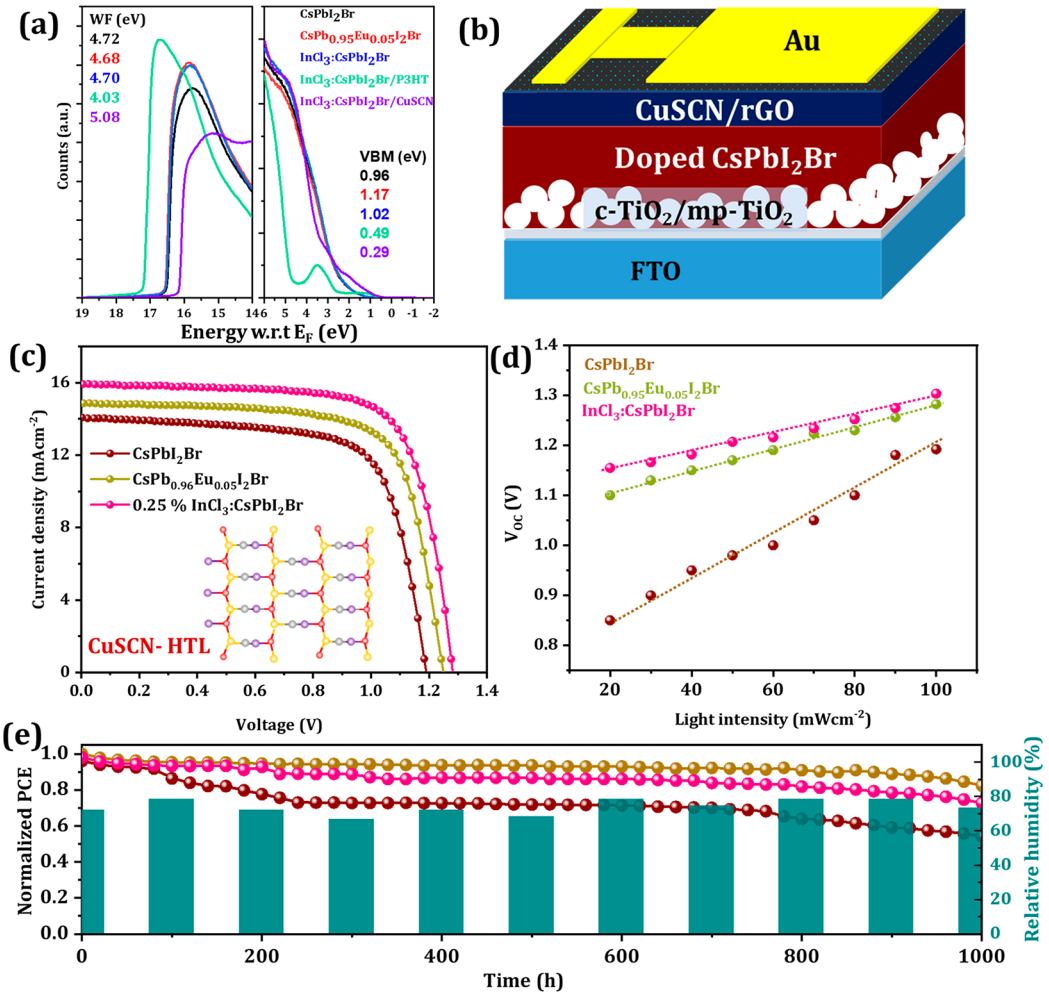

Figure 3. Dopant-free CuSCN HTL-based all-inorganic PSCs. (a) Ultraviolet photoelectron spectroscopy (UPS) spectra (using the He−I line with photon energy of 21.22 eV) corresponding to the secondary electron onset region (WF, work function) and valence band region (VBM, valence band minimum) of the as-prepared $CsPbI_2Br$, $CsPb_{0.95}Eu_{0.05}I_2Br$, and 0.25% $InCl_3$:$CsPbI_2Br$ and in contact with P3HT and CuSCN (HTL) with respect to the Fermi energy (w.r.t. E_F). VBM onsets for perovskites were determined from semilog plots (Figure S13). (b) Device architecture based on CuSCN HTL. (c) J−V characteristics. (d) Intensity-dependent V_{OC} variation of respective devices. (e) Normalized PCE (*for at least 5 devices for each composition*) monitored at 85 °C in ambient air conditions at 65−75% RH.

PLQY analysis, we can directly observe an increase in the quasi-Fermi level splitting (QFLS) which leads to improved device performance through an increase in V_{OC}.[51−54] The change in the QFLS (herein ΔQFLS) for solar cell materials has been calculated previously (Supporting Note 3).[50] Figure 2b and Tables S2 and S3 show the detailed PLQY parameters of the bare and doped $CsPbI_2Br$ thin films in contact with HTL and ETLs. We observe improvement in the ΔPLQY values after Eu^{2+} or In^{3+} doping in the presence of both HTL and ETLs and also substantial gains for the $CsPbI_2Br$ thin films coated on TiO_2 ETL, indicating nonradiative recombination in the n-i-p devices is the main factor limiting the open-circuit voltage. The PLQY is nearly 2 and 3 times larger for Eu- and In-doped films, respectively, with the expected gain of ΔQFLS = 21.78 and 22.68 meV at the TiO_2/perovskite interface. Therefore, the doped samples are expected to exhibit enhanced V_{OC} once implemented in complete devices. Emission lifetimes are extracted from the fluorescence-lifetime imaging microscopic (FLIM) images in Figure S5. TRPL decay profiles (Figure S5b) were measured at ∼640 nm to examine the kinetics of photogenerated excitons and free carriers. Parameters extracted from triexponential fitting are provided in Table S4, Supporting Note 4.[55,56] The $CsPbI_2Br$, $CsPb_{095}Eu_{0.05}I_2Br$, and 0.25% $InCl_3$:$CsPbI_2Br$ thin film compositions exhibit extensions in average lifetime $\langle\tau_{avg}\rangle$ from 2.03 to 27 and 16 ns, respectively. The elongation of the PL decay can be ascribed to the synergetic effect of dense morphology, reduced grain boundary, compactness, limited defects, and metal ion-doped perovskite films.

Next, to investigate Eu^{2+}, In^{3+}, and Cl^- incorporation within the perovskite lattice, we performed X-ray photoelectron spectroscopy (XPS) (Figures 2c−f and S6−S8). All samples exhibited Cs 3d, Pb 4f, I 3d, and Br 3d core levels at characteristic binding energies.[57] However, we observed that the Pb 4f, I 3d, and Br 3d peaks are shifted to lower binding energy for $CsPb_{0.95}Eu_{0.05}I_2Br$ samples, which is due to the formation of new Pb−X−Eu (X: Br and I) chemical bonding. Notably, the Cs 3d peak shows a negligible shift after Eu doping because of weak interaction between Cs^+ and the central atom (Eu) in the octahedron (see Supporting Note 5 and Table S2) (Figure 2d).[58,59] For the case of In-Cl_3:$CsPbI_2Br$, apart from the parent element signatures (*i.e.*, Cs^+, Pb^{2+}, I^-, and Br^-), the presence of In 3d (In $3d_{5/2}$, 445.16; In $3d_{3/2}$, 452.67 eV) and Cl 2p (200.79 eV) peaks confirms

https://dx.doi.org/10.1021/acsenergylett.0c02385
ACS Energy Lett. 2021, 6, 778−788

Table 1. Photovoltaic Performance Outcomes of Cells Fabricated from DHA Methods with Divalent (Eu^{2+}) and Trivalent (In^{3+}) Metal Ion-Doped $CsPbI_2Br$ All-Inorganic Perovskites Using Dopant-Free CuSCN and P3HT HTLs

sample	HTL	V_{OC} (V)	J_{SC} (mA cm^{-2})	FF (%)	PCE (%)
$CsPbI_2Br$ $_{(average)}$	CuSCN	1.185	13.80	70.00	11.45
$CsPbI_2Br$ $_{(champion)}$		1.192	14.06	71.68	12.01
$CsPb_{0.95}Eu_{0.05}I_2Br_{(average)}$		1.235	14.45	72.00	12.84
$CsPb_{0.95}Eu_{0.05}I_2Br_{(champion)}$		1.249	14.90	73.76	13.72
0.25% $InCl_3$:$CsPbI_2Br_{(average)}$		1.275	15.55	74.5	14.77
0.25% $InCl_3$:$CsPbI_2Br_{(champion)}$		1.282	15.91	74.85	15.27
0.25% $InCl_3$:$CsPbI_2Br$ $_{(average)}$	P3HT	1.295	15.65	74.50	15.09
0.25% $InCl_3$:$CsPbI_2Br_{(champion)}$		1.303	15.90	75.76	15.69

that In^{3+} and Cl^- are incorporated in the parent $CsPbI_2Br$ lattice (Figure 2e,f). Similar to the $CsPb_{0.95}Eu_{0.05}I_2Br$ sample, we have also observed a corresponding shift in the Pb 4f, I 3d, and Br 3d peaks to lower binding energies, again being ascribed to the formation of new Pb−X−In (X: Br and I) bonds. It is also noted that the shift will remain relatively small because of the small amount of doping involved (0.25% $InCl_3$ doping concentration).[46] Conversely, 2% $InCl_3$:$CsPbI_2Br$ samples exhibited much more pronounced shifts, which evidently supports successful introduction of In (Figure S9 and Table S6.)

Furthermore, high-angle annular dark-field scanning transmission electron microscopy (HAADF-STEM) mapping of the $CsPb_{0.95}Eu_{0.05}I_2Br$ and $InCl_3$:$CsPbI_2Br$ sample showed that the Eu^{2+} and In^{3+}, along with Cl^-, are distributed uniformly within the perovskite grains at the atomic level. In addition, the uniformity of all other Cs, Pb, I, and Br elements is seen (Figures S10 and S11). Both XPS and HAAD-STEM analysis revealed that both Eu^{2+} and In^{3+} along with Cl^- are incorporated evenly within the parent $CsPbI_2Br$ lattice.

The UV−vis optical absorption spectra of the perovskite thin films deposited on the FTO/c-TiO_2/mp-TiO_2 substrate are shown in Figure S12. Black-phase $CsPbI_2Br$ shows an absorption edge (~640 nm/1.91 eV) which is slightly blue-shifted by the incorporation of the Eu^{2+} and nearly without shift because of In^{3+} inclusion.[32,46] The electronic structures of the various layers were characterized by ultraviolet photoemission spectroscopy (UPS) (Figures 3a and S13). The work function (WF) and valence band maximum (VBM) were calculated from the binding energy cutoff (E_{cutoff}) and the binding energy onset (E_{onset}). The corresponding WF values of each layer were estimated to be 4.72, 4.68, 4.70, 4.03, and 5.08 eV for $CsPbI_2Br$, $CsPb_{0.95}Eu_{0.05}I_2Br$, $InCl_3$:$CsPbI_2Br$, $InCl_3$:$CsPbI_2Br$/P3HT, and $InCl_3$:$CsPbI_2Br$/CuSCN samples, respectively (Table S7). The VBM and CBM positions after Eu and $InCl_3$ doping did not change drastically, while the WF shifted by 210 and 60 meV toward the CB after Eu and $InCl_3$ doping, respectively. These results indicate the presence of additional negative charge carriers after Eu or In doping. Further, Eu and $InCl_3$ incorporation improved the energy level alignment of the conduction band minimum between the doped $CsPbI_2Br$ perovskites and the ETL (Figure S14). Energy level diagrams revealed the P3HT and CuSCN, with respect to doped $CsPbI_2Br$, matched favorably, resulting in efficient hole transportation. Therefore, it is expected that at the interface charge accumulation loss will be reduced and will help to improve the built-in potential across the perovskite film, resulting in higher V_{OC} of the doped-$CsPbI_2Br$-based devices.

We pursue devices which have all of their layers deposited, annealed, and studied in an open atmosphere (except for gold deposition). Initially, we fabricated solar cells having the standard bilayered n-i-p device configuration, FTO/c-TiO_2/mp-TiO_2/$CsPbI_2Br$/CuSCN/Au (Figure 3a). For comparison, we also fabricated identical devices using $CsPb_{0.95}Eu_{0.05}I_2Br$ and 0.25% $InCl_3$:$CsPbI_2Br$ based on CuSCN HTL. The dopant-free CuSCN HTL has been deposited on annealed $CsPbI_2Br$ perovskite thin film by a dynamic spin coating method from 35 mg mL^{-1} DES solvent followed by rGO deposition.[60,38] Figure 3c shows the $J-V$ characteristics of CuSCN-based $CsPbI_2Br$ PSCs. The cross-sectional SEM images of the doped $CsPbI_2Br$ thin films exhibit improved capping layer thickness from 300, 350 to 375 nm respectively for controlled, Eu^{2+} and $InCl_3$-doped perovskite thin films (Figure S15). Interestingly, no grain boundaries in the cross-sectional image are observed, but rather we see the formation of a single crystalline-like layer.[61] The perovskite device based on $CsPbI_2Br$ perovskite film with CuSCN HTL delivers 12.01% PCE with V_{OC} of 1.192 V, short-circuit current density (J_{SC}) of 14.06 $mAcm^{-2}$, and fill factor (FF) of 71.68%. In contrast, devices based on $CsPb_{0.95}Eu_{0.05}I_2Br$ and $InCl_3$:$CsPbI_2Br$ have increased V_{OC} and J_{SC}, because of improved thickness and film quality. The optimized devices having FTO/c-TiO_2/mp-TiO_2/$CsPb_{0.95}Eu_{0.05}I_2Br$/CuSCN/Au exhibits V_{OC} of 1.249 V, J_{SC} of 14.90 mA cm^{-2}, and FF of 73.76% and results in PCE of 13.72%. From cross-sectional SEM images, it is observed that both TiO_2/perovskite and perovskite/CuSCN interfaces are highly uniform, void-free, and smooth.

Interestingly, the hot-air method resulted in a >500 nm-thick layer which is typically difficult to achieve using conventional solution processing methods. For the case of trivalent In^{3+} and Cl^- codoping, the V_{OC} is slightly higher than in the other devices and reaches 1.282 V with J_{SC} of 15.91 $mAcm^{-2}$ and FF of 74.85% resulting in 15.27% PCE (Table 1). This improved performance is also reflected in the external quantum efficiency (EQE) spectra of $CsPbI_2Br$, $CsPb_{0.95}Eu_{0.05}I_2Br$, and $InCl_3$:$CsPbI_2Br$-based devices (Figure S16). Our champion device based on $InCl_3$:$CsPbI_2Br$ produces ~90% EQE values, giving J_{int} of 15.20 $mAcm^{-2}$, which approaches the current values measured from $J-V$ curves.

Furthermore, the stabilized power output (SPO) of the champion devices were monitored for full sun illumination over 200 s (Figure S17). The steady-state photocurrent outputs for the $CsPbI_2Br$-, $CsPb_{0.95}Eu_{0.05}I_2Br$-, and $InCl_3$:$CsPbI_2Br$-based devices are 14.30, 14.63, and 15.64 $mAcm^{-2}$, respectively, and all exhibit J_{SC} values close to those obtained from $J-V$ curves. The steady-state output values yielded stabilized PCE values of 12.02%, 13.61%, and

https://dx.doi.org/10.1021/acsenergylett.0c02385
ACS Energy Lett. 2021, 6, 778−788

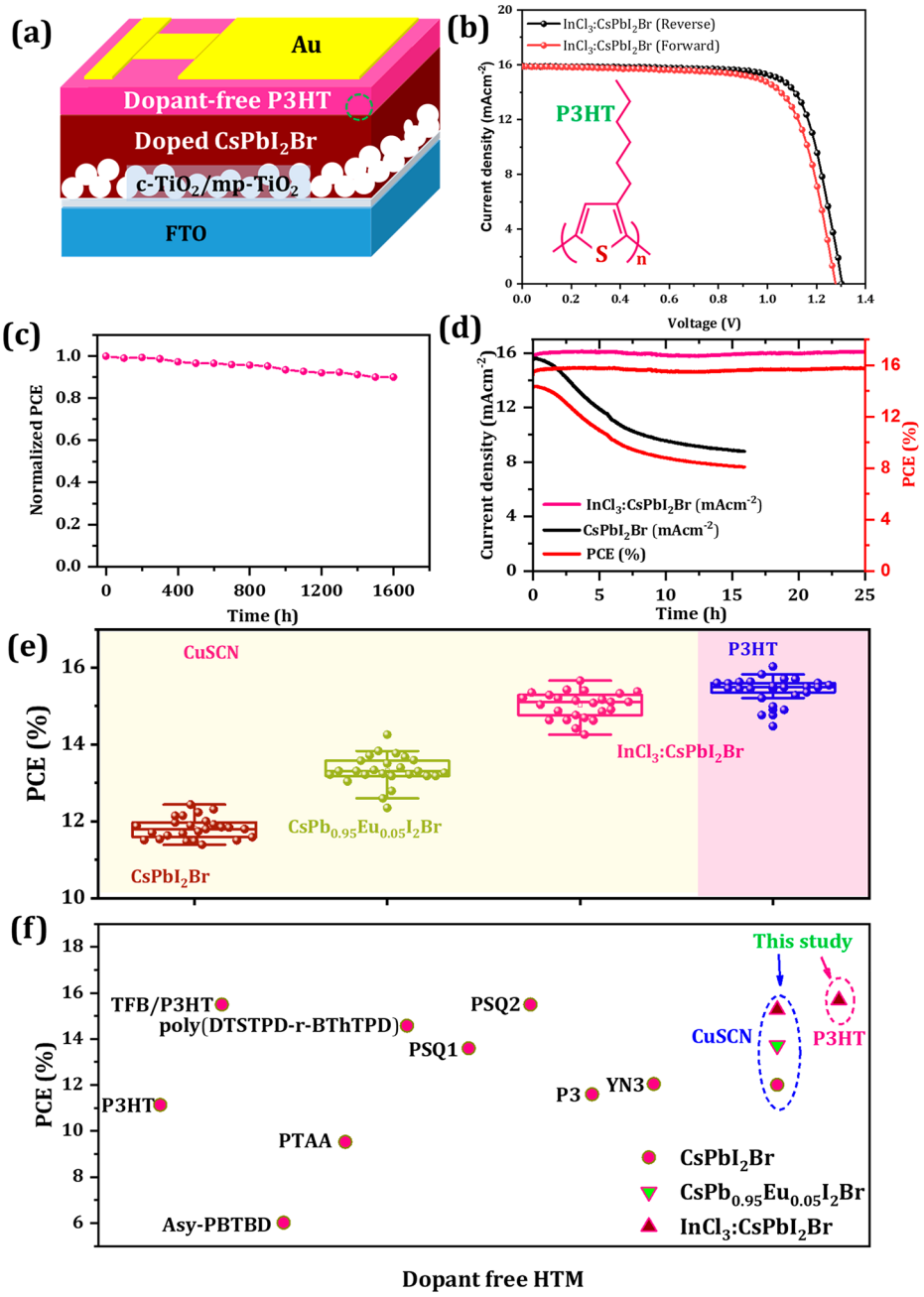

Figure 4. (a) Dopant-free P3HT HTL-based device configuration. (b) *J*–*V* characteristics of $InCl_3$:$CsPbI_2Br$-based solar cells using dopant-free P3HT. (c) Ambient conditions device stability at 40–50% RH at 85 °C thermal stress of the 5 devices. (d) Steady-state current density and PCE of unencapsulated $CsPbI_2Br$ and $InCl_3$:$CsPbI_2Br$ devices monitored under continuous 1.5 AM solar-simulator illumination as a function of time. (e) Device performance distribution for dopant-free HTLs for $InCl_3$:$CsPbI_2Br$-based PSCs. (f) Distribution of PCE based on different dopant-free HTLs reported to date. Data has been extracted from refs 40, 43, 65, and 65.

15.10% for $CsPbI_2Br$-, $CsPb_{0.95}Eu_{0.05}I_2Br$-, and $InCl_3$:$CsPbI_2Br$-based devices, respectively. In contrast, the current density output of the bare $CsPbI_2Br$-based devices declined continuously, whereas the $CsPb_{0.95}Eu_{0.05}I_2Br$ and $InCl_3$:$CsPbI_2Br$-based devices persisted far longer. This stabilized performance arises from the incorporation of metal cation doping, which stabilizes the photoactive black-phase (mechanism outlined below) and reduces the nonradiative recombination.

For charge transport measurements, we recorded the V_{OC} as a function of illumination intensity for the examined perovskite devices (Figure 3d). The slope of the fitted data yields the ideality factor (η), which was determined by $V_{OC} = nkT\ln(I)/q + A$, where k, T, and q are Boltzmann constant, the temperature in Kelvin, and the elementary charge, respectively. Parameter A is a constant according to the Shockley–Read–Hall (SRH) recombination mechanism.[62−64] The above equation can be simplified for η as, η = slope × $\frac{q}{kT}$. It is considered that the trap-assisted recombination played a dominant role in determining the characteristics of devices at η = 2. Our controlled device gives η values as high as 1.52, which decreased to 1.23 and 1.15 for $CsPb_{0.95}Eu_{0.05}I_2Br$ and 0.25% $InCl_3$:$CsPbI_2Br$-based devices, respectively, indicating the suppression of charge recombination.

https://dx.doi.org/10.1021/acsenergylett.0c02385
ACS Energy Lett. 2021, 6, 778−788

Next, we monitored hysteresis and found control devices exhibited PCE values of 11.09% and 12.01% for the forward and reverse scans, respectively (Figure S18). In contrast, the $CsPb_{0.95}Eu_{0.05}I_2Br$-based device exhibited 12.51% and 13.72% PCE in forward and reverse scan which is reduced because of highly uniform film quality. Further, we have also monitored the device performance of our champion $InCl_3$:$CsPbI_2Br$-based devices which exhibited J_{SC} of 15.61 mA cm^{-2}, V_{OC} of 1.262 V, and FF of 72.42%, resulting in PCE of 14.26% in the forward scan. On the other hand, the reverse scan exhibited 15.27% PCE with J_{SC} of 15.91 mA cm^{-2}, V_{OC} of 1.282 V, and FF of 74.85%; Table S8 indicates less hysteresis than the control architecture.

We selected the best performing devices from each composition and studied the air-stability of unencapsulated devices under continuous white light LED illumination, equivalent to 100 mW cm^{-2} in an ambient condition at 85 °C thermal stress. All devices were monitored under identical conditions; however, we have not regulated the environmental monitoring/control throughout the measurements. The stability analysis of these champion devices exhibited higher device performance due to excellent thermal stability properties of CuSCN HTL (Figure 3e). The bare $CsPbI_2Br$-based device maintained ∼60% initial efficiency after 1000 h; however, In^{3+} and Eu^{2+} incorporated devices retain over 75% and 87%, respectively, indicating excellent device stability.

P3HT is another low-cost HTL and can be used without any additive dopants, and we further examine its suitability for our developed champion $InCl_3$:$CsPbI_2Br$ absorber composition (Figure 4a).[42] These devices exhibited 14.83% (with V_{OC} = 1.277 V, J_{SC} = 15.90 $mAcm^{-2}$, and FF = 73.10%) and 15.69% (with V_{OC} = 1.303 V, J_{SC} = 15.91 $mAcm^{-2}$, and FF = 75.76%) for forward and reverse scans, respectively (Figure 4b and Table S9). The stability analysis revealed the P3HT devices also retain >95% of initial PCE over 1600 h, indicating excellent ambient stability under 85 °C thermal stress (Figure 4c). The photostability under 1 sun continuous illumination for several hours indicated the doped sample exhibited excellent photostability as compared to the control device (Figure 4d). The $InCl_3$:$CsPbI_2Br$/P3HT champion unencapsulated device was sent for third-party efficiency testing and was confirmed to exhibit a certified 14.97% PCE (see Figure S19).

For comparison, we have also fabricated conventional additive-doped spiro-MeOTAD-based devices and monitored their ambient stability (Figure S20). Unfortunately, even though we used expensive additive-based spiro-MeOTAD HTL, it shows lower efficiency. The best-performing device exhibited 13.70% PCE with V_{OC} = 1.197 V, J_{SC} = 15.81 $mAcm^{-2}$, and FF = 72.42%. This may be linked to the deposition of spiro-MeOTAD-based HTL under ambient conditions and its moisture instability. The ambient stability monitored under ambient conditions revealed sharp drops up to 50% within a few hours and retained only ∼20% of the initial PCE only after 100 h. This is due to the sensitive nature of additives-doped Spiro-MeOTAD HTL. Furthermore, we fabricated dopant-free spiro-MeOTAD-based devices, but these devices showed limited PCE (Figure S21).

Figures 4e and S22 show the statistical distribution of the PCEs in forward and reverse scan based on different compositions and methods. The statistical distribution of the PCE revealed high repeatability of the device performance. Interestingly, the reproducibility of the Eu^{2+}- and In^{3+}-doped $CsPbI_2Br$-based devices were better in comparison to those prepared with the bare $CsPbI_2Br$ compositions. For instance, in the $CsPbI_2Br$-based devices, we observed an average PCE of ∼12.2% with V_{OC} of 1.18 ± 0.01 V, J_{SC} of 14.21 $mAcm^{-2}$, and FF of 72 ± 2%; however, the $CsPb_{0.95}Eu_{0.05}I_2Br$-based devices exhibited excellent reproducibility with V_{OC} of 1.250 ± 0.01 V, J_{SC} of 15.30 ± 0.5 $mAcm^{-2}$, and FF of 73 ± 2% yielding average efficiency >13.50 ± 0.1%. As expected, all 0.25% $InCl_3$:$CsPbI_2Br$-based devices exhibited higher current density with V_{OC} exceeding 1.30 V, which is due to the synergistic effect of hot-air method, metal-ion doping, and the suitability of the HTL.

We believe that our hot-air processed devices also exhibited state-of-the-art power conversion efficiency for dopant-free HTL-based devices (Figure 4f).[65,66] We conclude that although there are a range of deposition methods and different dopant-free HTLs which can be explored, our combination of hot-air method with low-cost, dopant-free CuSCN and P3HT HTL-based devices embodies a promising route for high-efficiency devices that can be both processed and operated under fully ambient conditions. Among the previous methods used for inorganic perovskite solar cells to date, our work showed a record PCE of 15.69% for $InCl_3$:$CsPbI_2Br$ composition and dopant-free P3HT HTL.

The stabilizing mechanism of metal doping in the normally unstable $CsPbI_2Br$ parent perovskite system is yet to be discussed. Within a moisture-rich ambient atmosphere, water acts as a catalyst toward phase decay and δ-phase (non-perovskite) formation, partially dissolving the surface halide anions and introducing vacancies.[67] As a result, the increased concentration of surface halide vacancies lowers the kinetic barrier and accelerates phase degradation, *i.e.* turning into the δ-phase. This is clearly tracked in Figures S23 and S24, showing the decay of the bare $CsPbI_2Br$ perovskite thin films within hours of ambient storage. A complete transformation of the perovskite into the δ-phase is confirmed via structural refinement of the XRD patterns recorded after degradation, confirming the absence of any detectable crystalline side-products. This confirmed that the degradation mechanism under an ambient atmosphere is perovskite phase destabilization. The incorporation of $InCl_3$ does little to slow a similar degradation pathway in an exposed thin film (*i.e.*, no top contact layers attached); however, Eu is relatively successful in preserving the perovskite phase under the same conditions.

The change in stability cannot be accounted for purely based on a model which considers changes to the lattice tolerance factor, whereby reducing the unit cell volume (via B site doping) can increase the tolerance factor when the A and X sites remain unchanging. Similar stabilizing effects have been demonstrated recently for $CsPbI_3$ doped with a few percent of Bi^{3+}.[68]

For phase transitions in which the high-symmetry α-phase is reduced to a degenerate γ-phase, the number of distortion components can be expressed in terms of symmetry-adapted strains.[69,15] The decoupled strain components are presented in Figure S25 (Supporting Note 6). Starting with a bare γ-$CsPbI_2Br$ perovskite, both $InCl_3$ and Eu doping suppress the strain-related distortions in the perovskite crystal, making it more cubic-like (*i.e.*, α-phase). Like the stabilizing effect of heating $CsPbI_2Br$ toward a stable cubic perovskite structure, we suggest that the doping stabilizes the system because of a reversal of the spontaneous strains leading to phase decay. In addition, this effect is the largest for the Eu system, which we

https://dx.doi.org/10.1021/acsenergylett.0c02385
ACS Energy Lett. 2021, 6, 778−788

find is the most stable when used in an ambient-stable device.[70] Furthermore, we have recorded focused ion beam (FIB) cross-sectional images of the fabricated devices using the $CsPbI_2Br$-based absorbers (Figure S26). To study degradation, we have obtained FIB images of the fresh devices (~10 h after fabrication) and after 14 days of aging. The FIB images of the freshly prepared devices exhibited formation of compact capping layers onto mp-TiO_2 ETL. Interestingly, the P3HT layer is uniformly deposited and the perovskite/P3HT interface is smooth. In the present investigation, we have used doped $CsPbI_2Br$ perovskite compositions, which is free from conventional organic cations such as MAI, FAI, or DMAI. Therefore, there is less possibility of the formation of HI gases during degradation. However, we observed the formation of bright spots and dark voids in the $CsPbI_2Br$-based materials, which revealed iodine degradation or halide ion-migration and the formation of δ-$CsPbI_2Br$ or PbI_2.[71] This is the most likely degradation of the bare $CsPbI_2Br$-based devices. On the other hand, our $CsPb_{0.95}Eu_{0.05}I_2Br$- and $InCl_3$:$CsPbI_2Br$-based devices exhibit an intact morphology of the capping layer even though we recorded them on devices aged for 14 days, indicating the devices were well-preserved.

In summary, we have utilized a simple hot-air method for the fabrication of high-quality $CsPbI_2Br$ thin films under ambient conditions. Our control over the deposition and the incorporation of Eu and In cations offers a new approach for stabilization of a functional $CsPbI_2Br$ black-phase in ambient air. The XRD, XPS, and STEM-HAADF analyses evidenced that the Eu and In cations are successfully incorporated into $CsPbI_2Br$ crystal which inhibits the black-to-yellow phase transformation by releasing spontaneous strains in the lattice. Our TRPL measurements revealed longer carrier life times due to Eu and In incorporation, indicating the passivation of traps. The fabricated $InCl_3$:$CsPbI_2Br$-based PSCs devices based on dopant-free, low-cost CuSCN and P3HT HTLs exhibited record PCEs of 15.27% and 15.69%, respectively. Long-term thermal analysis revealed more than 95% retention over 1600 h of operation under ambient conditions, which is much greater than the conventional additives-doped Spiro-MeOTAD HTL. We believe that our hot-air processed devices exhibited state-of-the-art power conversion efficiency in dopant-free HTL-based PSCs. These results provide new insights for the fabrication of high-quality cesium-based PSCs and low-cost dopant-free HTLs with excellent efficiency and air−thermal stability.

■ ASSOCIATED CONTENT

Supporting Information

The Supporting Information is available free of charge at https://pubs.acs.org/doi/10.1021/acsenergylett.0c02385.

Full experimental procedures and device fabrication, DFT analysis details, materials, experimental methods, materials' characterization, detailed discussion on methods and XPS analysis, PLQY calculations, TRPL analysis, HAADF-STEM, FIB, stability analysis, and testing (PDF)

■ AUTHOR INFORMATION

Corresponding Authors

Sawanta S. Mali − *Polymer Energy Materials Laboratory, School of Advanced Chemical Engineering, Chonnam National University, Gwangju, South Korea 61186;* orcid.org/0000-0002-4973-4203; Email: sawanta@jnu.ac.kr

Chang Kook Hong − *Polymer Energy Materials Laboratory, School of Advanced Chemical Engineering, Chonnam National University, Gwangju, South Korea 61186;* Email: hongck@jnu.ac.kr

Authors

Jyoti V. Patil − *Polymer Energy Materials Laboratory, School of Advanced Chemical Engineering, Chonnam National University, Gwangju, South Korea 61186; Optoelectronic Convergence Research Center (OCRC), Chonnam National University, Gwangju, South Korea 61186;* orcid.org/0000-0003-1269-3767

Julian A. Steele − *cMACS, Department of Microbial and Molecular Systems, KU Leuven, 3001 Leuven, Belgium;* orcid.org/0000-0001-7982-4413

Sachin R. Rondiya − *School of Chemistry, Cardiff University, Cardiff CF10 3AT, United Kingdom;* orcid.org/0000-0003-1350-1237

Nelson Y. Dzade − *School of Chemistry, Cardiff University, Cardiff CF10 3AT, United Kingdom;* orcid.org/0000-0001-7733-9473

Complete contact information is available at: https://pubs.acs.org/10.1021/acsenergylett.0c02385

Author Contributions

S.S.M. and C.K.H. contributed to the conception and design of the experiments. S.S.M. fabricated all the devices and conducted most of the characterizations. S.S.M. and C.K.H. wrote the manuscript. J.V.P. and G.M. participated in writing the manuscript. S.S.M., S.R.R., and N.Y.D. carried out DFT analysis and discussed results. J.A.S. carried out XRD refinement and analysis. All authors discussed the results and reviewed the manuscript.

Notes

The authors declare no competing financial interest.

■ ACKNOWLEDGMENTS

This work was supported by the Korea Research Fellowship Program through the National Research Foundation of Korea (NRF) funded by the Ministry of Science, ICT, and Future Planning (2016H1D3A1909289) for awarding an outstanding overseas young researcher to S.S.M. This work was also supported by Korea Research Fellowship Program through the National Research Foundation of Korea (NRF) (2020R1A2C2004880). This research is also supported by the National Research Foundation of Korea (NRF) (NRF-2017R1A2B4008117) and (NRF-2018R1A6A1A03024334). This work was also supported by the National Research Foundation of Korea (NRF) grant funded by the Korea government (MSIT) (2018R1C1B6008218). J.A.S. acknowledges financial support from the Research Foundation - Flanders (FWO: Grant No. 12Y7221N). The authors thank Mrs. Young Hee Jung for providing FIB analysis. Authors would like to thank Prof. Gustavo de Miguel for valuable discussion on UV-vis absorption analysis and valuable suggestions during preparation and revision of this manuscript. S.R.R. and N.Y.D. acknowledge the UK Engineering and Physical Sciences Research Council (EPSRC) for funding (Grant No. EP/S001395/1). This work made use of the ARCHER UK National Supercomputing Service (http://

www.archer.ac.uk) via our membership of the UK's HEC Materials Chemistry Consortium, which is also funded by the EPSRC (EP/L000202). The computational facilities of the Advanced Research Computing at Cardiff (ARCCA) Division, Cardiff University, and HPC Wales were also used in the completion of this work.

REFERENCES

(1) National Renewable Energy Laboratory Solar efficiency chart. https://www.nrel.gov/pv/assets/pdfs/best-research-cell-efficiencies.20200929.pdf (accessed: 2020-09-29).
(2) Burschka, J.; Pellet, N.; Moon, S. J.; Humphry-Baker, R.; Gao, P.; Nazeeruddin, M. K.; Gratzel, M. Sequential Deposition as a Route to High-Performance Perovskite-Sensitized Solar Cells. *Nature* **2013**, *499*, 316−319.
(3) Kim, H.-S.; Lee, C.-R.; Im, J.-H.; Lee, K.-B.; Moehl, T.; Marchioro, A.; Moon, S.-J.; Humphry-Baker, R.; Yum, J.-H.; Moser, J. E.; Gratzel, M.; Park, N.-G. Lead Iodide Perovskite Sensitized All-Solid-State Submicron Thin Film Mesoscopic Solar Cell with Efficiency Exceeding 9%. *Sci. Rep.* **2012**, *2*, 591.
(4) Shin, S. S.; Yeom, E. J.; Yang, W. S.; Hur, S.; Kim, M. G.; Im, J.; Seo, J.; Noh, J. H.; Seok, S. I. Colloidally Prepared La-Doped $BaSnO_3$ Electrodes for Efficient, Photostable Perovskite Solar Cells. *Science* **2017**, *356*, 167−171.
(5) Jeon, N. J.; Na, H.; Jung, E. H.; Yang, T.-Y.; Lee, Y. G.; Kim, G.; Shin, H.-W.; Seok, S. I.; Lee, J.; Seo, J. A Fluorene-Terminated Hole-Transporting Material for Highly Efficient and Stable Perovskite Solar Cells. Nat. *Energy* **2018**, *3*, 682−689.
(6) Green, M. A.; Dunlop, E. D.; Hohl-Ebinger, J.; Yoshita, M.; Kopidakis, N.; Hao, X. Solar Cell Efficiency Tables (version 56). *Prog. Photovoltaics* **2020**, *28*, 629−638.
(7) Saliba, M.; Matsui, T.; Domanski, K.; Seo, J. Y.; Ummadisingu, A.; Zakeeruddin, S. M.; Correa-Baena, J. P.; Tress, W. R.; Abate, A.; Hagfeldt, A.; Grätzel, M. Incorporation of Rubidium Cations into Perovskite Solar Cells Improves Photovoltaic Performance. *Science* **2016**, *354*, 206−209.
(8) Habisreutinger, S. N.; McMeekin, D. P.; Snaith, H. J.; Nicholas, R. J. Research Update: Strategies for Improving the Stability of Perovskite Solar Cells. *APL Mater.* **2016**, *4*, 091503.
(9) Wu, S.; Li, Z.; Li, M. Q.; Diao, Y.; Lin, F.; Liu, T.; Zhang, J.; Tieu, P.; Gao, W.; Qi, F.; Pan, X.; Xu, Z.; Zhu, Z.; Jen, A. K.-Y. 2D Metal−Organic Framework for Stable Perovskite Solar Cells with Minimized Lead Leakage. *Nat. Nanotechnol.* **2020**, *15*, 934−940.
(10) Lin, Y. H.; et al. A Piperidinium Salt Stabilizes Efficient Metal-Halide Perovskite Solar Cells. *Science* **2020**, *369* (6499), 96−102.
(11) Stoumpos, C. C.; Malliakas, C. D.; Kanatzidis, M. G. Semiconducting Tin and Lead Iodide Perovskites with Organic Cations: Phase Transitions, High Mobilities, and Near-Infrared Photoluminescent Properties. *Inorg. Chem.* **2013**, *52*, 9019−9038.
(12) Eperon, G. E.; Paternò, G. M.; Sutton, R. J.; Zampetti, A.; Haghighirad, A. A.; Cacialli, F.; Snaith, H. J. Inorganic Caesium Lead Iodide Perovskite Solar Cells. *J. Mater. Chem. A* **2015**, *3*, 19688−19695.
(13) Wang, Y.; Liu, X.; Zhang, T.; Wang, X.; Kan, M.; Shi, J.; Zhaoe, Y. The Role of Dimethylammonium Iodide in $CsPbI_3$ Perovskite Fabrication: Additive or Dopant? *Angew. Chem., Int. Ed.* **2019**, *58*, 16691−16696.
(14) Wang, Y.; Dar, M. I.; Ono, L. K.; Zhang, T.; Kan, M.; Li, Y.; Zhang, L.; Wang, X.; Yang, Y.; Gao, X.; Qi, Y.; Grätzel, M.; Zhao, Y. Thermodynamically stabilized β-$CsPbI_3$−based perovskite solar cells with efficiencies > 18%. *Science* **2019**, *365* (6453), 591−595.
(15) Steele, J. A.; Lai, M.; Zhang, Y.; Lin, Z.; Hofkens, J.; Roeffaers, M. B. J.; Yang, P. Phase Transitions and Anion Exchange in All-Inorganic Halide Perovskites. *Acc. Mater. Res.* **2020**, *1* (1), 3−15.
(16) Goldschmidt, V. M. Die Gesetze der krystallochemie. *Naturwissenschaften* **1926**, *14*, 477.
(17) Sutton, R. J.; Eperon, G. E.; Miranda, L.; Parrott, E. S.; Kamino, B. A.; Patel, J. B.; Hörantner, M. T.; Johnston, M. B.; Haghighirad, A. A.; Moore, D. T.; Snaith, H. J. Bandgap-Tunable Cesium Lead Halide Perovskites with High Thermal Stability for Efficient Solar Cells. *Adv. Energy Mater.* **2016**, *6*, 1502458.
(18) Shah, A.; Torres, P.; Tscharner, R.; Wyrsch, N.; Keppner, H. Photovoltaic Technology: The Case for Thin-Film Solar Cells. *Science* **1999**, *285*, 692−698.
(19) Bremner, S. P.; Levy, M. Y.; Honsberg, C. B. Analysis of Tandem Solar Cell Efficiencies Under AM1.5G Spectrum Using a Rapid Flux Calculation Method. *Prog. Photovoltaics* **2008**, *16*, 225−233.
(20) Beal, R. E.; Slotcavage, D. J.; Leijtens, T.; Bowring, A. R.; Belisle, R. A.; Nguyen, W. H.; Burkhard, G. F.; Hoke, E. T.; McGehee, M. D. Cesium Lead Halide Perovskites with Improved Stability for Tandem Solar Cells. *J. Phys. Chem. Lett.* **2016**, *7* (5), 746−751.
(21) Swarnkar, A.; Marshall, A. R.; Sanehira, E. M.; Chernomordik, B. D.; Moore, D. T.; Christians, J. A.; Chakrabarti, T.; Luther, J. M. Quantum Dot-Induced Phase Stabilization of α-$CsPbI_3$ Perovskite for High-Efficiency Photovoltaics. *Science* **2016**, *354*, 92−95.
(22) Bian, H.; Bai, D.; Jin, Z.; Wang, K.; Liang, L.; Wang, H.; Zhang, J.; Wang, Q.; Liu, S. Graded Bandgap $CsPbI_{2+x}Br_{1-x}$ PerovskiteSolar Cells with a Stabilized Efficiency of 14.4%. *Joule* **2018**, *2*, 1500−1510.
(23) Luo, P.; Xia, W.; Zhou, S.; Sun, L.; Cheng, J.; Xu, C.; Lu, Y. Solvent Engineering for Ambient-Air-Processed, Phase-Stable $CsPbI_3$ in Perovskite Solar Cells. *J. Phys. Chem. Lett.* **2016**, *7*, 3603−3608.
(24) Jiang, Y.; Yuan, J.; Ni, Y.; Yang, J.; Wang, Y.; Jiu, T.; Yuan, M.; Chen, J. Reduced-Dimensional α-$CsPbX_3$ Perovskites for Efficient and Stable Photovoltaics. *Joule* **2018**, *2*, 1356−1368.
(25) Liang, J.; Zhao, P.; Wang, C.; Wang, Y.; Hu, Y.; Zhu, G.; Ma, L.; Liu, J.; Jin, Z. $CsPb_{0.9}Sn_{0.1}IBr_2$ Based All-Inorganic Perovskite Solar Cells with Exceptional Efficiency and Stability. *J. Am. Chem. Soc.* **2017**, *139*, 14009−14012.
(26) Zhang, T.; Dar, M. I.; Li, G.; Xu, F.; Guo, N.; Grätzel, M.; Zhao, Y. Bication lead iodide 2D perovskite component to stabilize inorganic α-$CsPbI_3$ perovskite phase for high-efficiency solar cells. *Sci. Adv.* **2017**, *3*, No. e1700841.
(27) Lau, C. F. J.; Deng, X.; Zheng, J.; Kim, J.; Zhang, Z.; Zhang, M.; Bing, J.; Wilkinson, B.; Hu, L.; Patterson, R.; Huang, S.; Ho-Baillie, A. Enhanced Performance via Partial Lead Replacement with Calcium for a $CsPbI_3$ Perovskite Solar Cell Exceeding 13% Power Conversion Efficiency. *J. Mater. Chem. A* **2018**, *6*, 5580−5586.
(28) Bai, D.; Zhang, J.; Jin, Z.; Bian, H.; Wang, K.; Wang, H.; Liang, L.; Wang, Q.; Liu, S. F. Interstitial Mn^{2+}-Driven High-Aspect-Ratio Grain Growth for Low-Trap-Density Microcrystalline Films for Record Efficiency $CsPbI_2Br$ Solar Cells. *ACS Energy Lett.* **2018**, *3*, 970−978.
(29) Lau, C. F. J.; Zhang, M.; Deng, X.; Zheng, J.; Bing, J.; Ma, Q.; Kim, J.; Hu, L.; Green, M. A.; Huang, S.; Ho-Baillie, A. Strontium Doped Low-Temperature-Processed $CsPbI_2Br$ Perovskite Solar Cells. *ACS Energy Lett.* **2017**, *2*, 2319−2325.
(30) Hu, Y.; Bai, F.; Liu, X.; Ji, Q.; Miao, X.; Qiu, T.; Zhang, S. Bismuth Incorporation Stabilized α-$CsPbI_3$ for Fully Inorganic Perovskite Solar Cells. *ACS Energy Lett.* **2017**, *2*, 2219−2227.
(31) Xiang, S.; Li, W.; Wei, Y.; Liu, J.; Liu, H.; Zhu, L.; Chen, H. The synergistic effect of non-stoichiometry and Sb-doping on air-stable α-$CsPbI_3$ for efficient carbon-based perovskite solar cells. *Nanoscale* **2018**, *10*, 9996−10004.
(32) Xiang, W.; Wang, Z.; Kubicki, D. J.; Tress, W.; Luo, J.; Prochowicz, D.; Akin, S.; Emsley, L.; Zhou, J.; Dietler, G.; Grätzel, M.; Hagfeldt, A. Europium-Doped $CsPbI_2Br$ for Stable and Highly Efficient Inorganic Perovskite Solar Cells. *Joule* **2019**, *3*, 205.
(33) Mali, S. S.; Patil, J. V.; Hong, C. K. Hot-Air-Assisted Fully Air-Processed Barium Incorporated $CsPbI_2Br$ Perovskite Thin Films for Highly Efficient and Stable All-Inorganic Perovskite Solar Cells. *Nano Lett.* **2019**, *19* (9), 6213−6220.
(34) Mali, S. S.; Patil, J. V.; Hong, C. K. Simultaneous Improved Performance and Thermal Stability of Planar Metal Ion Incorporated $CsPbI_2Br$ All-Inorganic Perovskite Solar Cells Based on MgZnO Nanocrystalline Electron Transporting Layer. *Adv. Energy Mater.* **2020**, *10* (3), 1902708.

https://dx.doi.org/10.1021/acsenergylett.0c02385
ACS Energy Lett. 2021, 6, 778−788

(35) Patil, J. V.; Mali, S. S.; Hong, C. K. Efficient and Stable All-Inorganic Niobium-Incorporated $CsPbI_2Br$ Based Perovskite Solar Cells. *ACS Appl. Mater. Interfaces* **2020**, *12* (24), 27176−27183.
(36) Mali, S. S.; Patil, J. V.; Hong, C. K. Making air-stable all-inorganic perovskite solar cells through dynamic hot-air. *Nano Today* **2020**, *33*, 100880.
(37) Mali, S. S.; Patil, J. V.; Kim, H. J.; Luque, R.; Hong, C. K. Highly efficient thermally stable perovskite solar cells via Cs:NiOx/CuSCN double-inorganic hole extraction layer interface engineering. *Mater. Today* **2019**, *26*, 8−18.
(38) Mali, S. S.; Patil, J. V.; Hong, C. K. A 'Smart-Bottle' humidifier-assisted air-processed CuSCN inorganic hole extraction layer towards highly-efficient, large-area and thermally-stable perovskite solar cells. *J. Mater. Chem. A* **2019**, *7*, 10246−10255.
(39) Stolterfoht, M.; Caprioglio, P.; Wolff, C. M.; Márquez, J. A.; Nordmann, J.; Zhang, S.; Rothhardt, D.; Hörmann, U.; Amir, Y.; Redinger, A.; Kegelmann, L.; Zu, F.; Albrecht, S.; Koch, N.; Kirchartz, T.; Saliba, M.; Unold, T.; Neher, D. The impact of energy alignment and interfacial recombination on the internal and external open-circuit voltage of perovskite solar cells. *Energy Environ. Sci.* **2019**, *12*, 2778−2788.
(40) Öz, S.; Jena, A. K.; Kulkarni, A.; Mouri, K.; Yokoyama, T.; Takei, Iz.; Ünlü, F.; Mathur, S.; Miyasaka, T. Lead(II) Propionate Additive and a Dopant-Free Polymer Hole Transport Material for $CsPbI_2Br$ Perovskite Solar Cells. *ACS Energy Lett.* **2020**, *5* (4), 1292−1299.
(41) Guo, Z.; Jena, A. K.; Takei, I.; Kim, G. M.; Kamarudin, M. A.; Sanehira, Y.; Ishii, A.; Numata, Y.; Hayase, S.; Miyasaka, T. V_{OC} Over 1.4 V for Amorphous Tin-Oxide-Based Dopant-Free $CsPbI_2Br$ Perovskite Solar Cells. *J. Am. Chem. Soc.* **2020**, *142*, 9725−9734.
(42) Jung, E. H.; Jeon, N. J.; Park, E. Y.; Moon, C. S.; Shin, T. J.; Yang, T.-Y.; Noh, J. H.; Seo, J. Efficient, Stable and Scalable Perovskite Solar Cells Using Poly(3-hexylthiophene). *Nature* **2019**, *567*, 511−515.
(43) Li, M.-H.; Liu, S.-C.; Qiu, F.-Z.; Zhang, Z.-Y.; Xue, D.-J.; Hu, J.-S. High-Efficiency $CsPbI_2Br$ Perovskite Solar Cells with Dopant-Free Poly(3-hexylthiophene) Hole Transporting Layers. *Adv. Energy Mater.* **2020**, *10*, 2000501.
(44) Parida, B.; Ryu, J.; Yoon, S.; Lee, S.; Seo, Y.; Cho, J. S.; Kang, D.-W. Two-Step Growth of $CsPbI_{3-x}Br_x$ Films Employing Dynamic CsBr treatment: Toward All-Inorganic Perovskite Photovoltaics with Enhanced Stability. *J. Mater. Chem. A* **2019**, *7*, 18488−18498.
(45) Chen, R.; Hui, Y.; Wu, B.; Wang, Y.; Huang, X.; Xu, Z.; Ruan, P.; Zhang, W.; Cheng, F.; Zhang, W.; Yin, J.; Li, J.; Zheng, N. Moisture-tolerant and High-quality α-$CsPbI_3$ Films for Efficient and Stable Perovskite Solar Modules. *J. Mater. Chem. A* **2020**, *8*, 9597−9606.
(46) Liu, C.; Li, W.; Li, H.; Wang, H.; Zhang, C.; Yang, Y.; Gao, X.; Xue, Q.; Yip, H.-L.; Fan, J.; Schropp, R. E. I.; Mai, Y. Structurally Reconstructed $CsPbI_2Br$ Perovskite for Highly Stable and Square-Centimeter All-Inorganic Perovskite Solar Cells. Adv. *Energy Mater.* **2019**, *9*, 1803572.
(47) Li, X.; Wang, K.; Lgbari, F.; Dong, C.; Yang, W.; Ma, C.; Ma, H.; Wang, Z.-K.; Liao, L.-S. Indium Doped $CsPbI_3$ Films for Inorganic Perovskite Solar Cells with Efficiency Exceeding 17%. *Nano Res.* **2020**, *13*, 2203−2208.
(48) Miao, X.; Qiu, T.; Zhang, S.; Ma, H.; Hu, Y.; Bai, F.; Wu, Z. Air-stable $CsPb_{1-x}Bi_xBr_3$ ($0 \leq x \ll 1$) Perovskite Crystals: Optoelectronic and Photostriction Properties. *J. Mater. Chem. C* **2017**, *5*, 4931.
(49) De Mello, J. C.; Wittmann, H. F.; Friend, R. H. An Improved Experimental Determination of External Photoluminescence Quantum Efficiency. *Adv. Mater.* **1997**, *9* (3), 230−232.
(50) Robert, D. J.; Oliver; Lin, Y.-H.; Horn, A. J.; Xia, C. Q.; Warby, J. H.; Johnston, M. B.; Ramadan, A. J.; Snaith, H. J. Thermally Stable Passivation Toward High Efficiency Inverted Perovskite Solar Cells. *ACS Energy Lett.* **2020**, *5*, 3336−3343.
(51) Ross, R. T. Some Thermodynamics of Photochemical Systems. *J. Chem. Phys.* **1967**, *46* (12), 4590−4593.
(52) Miller, O. D.; Yablonovitch, E.; Kurtz, S. R. Strong Internal and External Luminescence as Solar Cells Approach the Shockley-Queisser Limit. *IEEE J. Photovoltaics* **2012**, *2* (3), 303−311.
(53) Stolterfoht, M.; Caprioglio, P.; Wolff, C. M.; Márquez, J. A.; Nordmann, J.; Zhang, S.; Rothhardt, D.; Hörmann, U.; Amir, Y.; Redinger, A.; Kegelmann, L.; Zu, F.; Albrecht, S.; Koch, N.; Kirchartz, T.; Saliba, M.; Unold, T.; Neher, D. The Impact of Energy Alignment and Interfacial Recombination on the Internal and External Open-Circuit Voltage of Perovskite Solar Cells. *Energy Environ. Sci.* **2019**, *12* (9), 2778−2788.
(54) Caprioglio, P.; Stolterfoht, M.; Wolff, C. M.; Unold, T.; Rech, B.; Albrecht, S.; Neher, D. On the Relation between the Open-Circuit Voltage and Quasi-Fermi Level Splitting in Efficient Perovskite Solar Cells. *Adv. Energy Mater.* **2019**, *9* (33), 1901631.
(55) Lakowicz, J. R. *Principles of Flurescence Spectroscopy*; 3rd ed.; Springer, 2006.
(56) Sillen, A.; Engelborghs, Y. The correct use of "Average" Fluorescence Parameters. *Photochem. Photobiol.* **1998**, *67*, 475−486.
(57) Wang, L.; Zhou, H.; Hu, J.; Huang, B.; Sun, M.; Dong, B.; Zheng, G.; et al. A Eu^{3+}-Eu^{2+} Ion Redox Shuttle Imparts Operational Durability to Pb-I Perovskite Solar Cells. *Science* **2019**, *363*, 265−270.
(58) Cho, E.-J.; Oh, S.-J. Surface Valence Transition in Trivalent Eu Insulating Compounds Observed by Photoelectron Spectroscopy. *Phys. Rev. B: Condens. Matter Mater. Phys.* **1999**, *59*, R15613.
(59) Yang, S.; Zhao, H.; Han, Y.; Duan, C.; Liu, Z.; Liu, S. Europium and Acetate Co-doping Strategy for Developing Stable and Efficient $CsPbI_2Br$ Perovskite Solar Cells. *Small* **2019**, *15*, 1904387.
(60) Arora, N.; Dar, M. I.; Hinderhofer, A.; Pellet, N.; Schreiber, F.; Zakeeruddin, S. M.; Grätzel, M. Perovskite Solar Cells with CuSCN Hole Extraction Layers Yield Stabilized Efficiencies Greater than 20%. *Science* **2017**, *358*, 768−771.
(61) Alsalloum, A. Y.; Turedi, B.; Zheng, X.; Mitra, S.; Zhumekenov, A. A.; Lee, K. J.; Maity, P.; Gereige, I.; AlSaggaf, A.; Roqan, I. S.; Mohammed, O. F.; Bakr, O. M. Low-Temperature Crystallization Enables 21.9% Efficient Single-Crystal $MAPbI_3$ Inverted Perovskite Solar Cells. *ACS Energy Lett.* **2020**, *5*, 657−662.
(62) Shuttle, C. G.; O'Regan, B.; Ballantyne, A. M.; Nelson, J.; Bradley, D. D. C.; Durrant, J. R. Bimolecular Recombination Losses in Polythiophene: Fullerene Solar Cells. *Phys. Rev. B: Condens. Matter Mater. Phys.* **2008**, *78*, 113201.
(63) Proctor, C. M.; Kuik, M.; Nguyen, T.-Q. Charge Carrier Recombination in Organic Solar Cells. *Prog. Polym. Sci.* **2013**, *38*, 1941−1960.
(64) Wang, H.; Hsu, J.-H.; Yang, G.; Yu, C. Novel Organic Schottky Barrier Diode Created in a Single Planar Polymer Film. Adv. *Adv. Mater.* **2016**, *28*, 9545−9549.
(65) Xiao, Q.; Tian, J.; Xue, Q.; Wang, J.; Xiong, B.; Han, M.; Li, Z.; Zhu, Z.; Yip, H.-L.; Li, Z. Dopant-Free Squaraine-Based Polymeric Hole-Transporting Materials with Comprehensive Passivation Effects for Efficient All-Inorganic Perovskite Solar Cells. *Angew. Chem., Int. Ed.* **2019**, *58*, 17724−17730.
(66) Zhang, D.; Xu, P.; Wu, T.; Ou, Y.; Yang, X.; Sun, A.; Cui, B.; Sun, H.; Hua, Y. Cyclopenta[*hi*]aceanthrylene-based dopant-free hole-transport material for organic−inorganic hybrid and all-inorganic perovskite solar cells. *J. Mater. Chem. A* **2019**, *7*, 5221−5226.
(67) Lin, J.; Lai, M.; Dou, L.; Kley, C. S.; Chen, H.; Peng, F.; Sun, J.; Lu, D.; Hawks, S. A.; Xie, C.; Cui, F.; Alivisatos, A. P.; Limmer, D. T.; Yang, P. Thermochromic Halide Perovskite Solar Cells. *Nat. Mater.* **2018**, *17*, 261−267.
(68) Hu, Y.; Bai, F.; Liu, X.; Ji, Q.; Miao, X.; Qiu, T.; Zhang, S. Bismuth Incorporation Stabilized α-$CsPbI_3$ for Fully Inorganic Perovskite Solar Cells. *ACS Energy Lett.* **2017**, *2*, 2219−2227.
(69) Putnis, A. *Introduction to Mineral Sciences*; Cambridge University Press: New York, 1992.
(70) Steele, J. A.; Solano, E.; Jin, H.; Prakasam, V.; Yuan, H.; Lin, Z.; Wang, Q.; Chernyshov, D.; Hofkens, J.; Roeffaers, M. B. J. Texture Formation in Polycrystalline Thin Films of All-Inorganic Lead Halide Perovskite. *arXiv* **2020**, 2010.14186 [cond-mat].

https://dx.doi.org/10.1021/acsenergylett.0c02385
ACS Energy Lett. 2021, 6, 778−788

(71) Yuan, H.; Debroye, E.; Janssen, K.; Naiki, H.; Steuwe, C.; Lu, G.; Moris, M.; Orgiu, E.; Uji, I. H.; De Schryver, F.; Samori, P.; Hofkens, J.; Roeffaers, M. Degradation of Methylammonium Lead Iodide Perovskite Structures Through Light and Electron Beam Driven Ion Migration. *J. Phys. Chem. Lett.* **2016**, *7*, 561−566.

https://dx.doi.org/10.1021/acsenergylett.0c02385
ACS Energy Lett. 2021, 6, 778−788